Progress In Electromagnetics Research, Vol. 150, 97–107, 2015

Resolution of the Frequency Diverse Metamaterial Aperture Imager

Okan Yurduseven[1, *], Mohammadreza F. Imani[1], Hayrettin Odabasi[1], Jonah Gollub[1], Guy Lipworth[1], Alec Rose[2], and David R. Smith[1, 3]

Abstract—The resolution of a frequency diverse compressive metamaterial aperture imager is investigated. The aperture consists of a parallel plate waveguide, in which an array of complementary, resonant metamaterial elements is patterned into one of the plates. Microwaves injected into the waveguide leak out through the resonant metamaterial elements, forming a spatially diverse waveform at the scene. As the frequency is scanned, the waveforms change, such that scene information can be encoded onto a set of frequency measurements. The compressive nature of the metamaterial imager enables image reconstruction from a significantly reduced number of measurements. We characterize the resolution of this complex aperture by studying the simulated point spread function (PSF) computed using different image reconstruction techniques. We compare the imaging performance of the system with that expected from synthetic aperture radar (SAR) limits.

1. INTRODUCTION

The use of microwaves for the detection and imaging of objects is of significant relevance to security applications due to the ability of microwaves to penetrate through materials that are not transparent at visible wavelengths. Because of this important capability, a considerable amount of research has been reported in the literature demonstrating the use of microwaves for various imaging applications, including medical imaging [1–4], through-wall imaging [5–8] and concealed ordnance imaging [9–12]. Most conventional imaging approaches employed in these applications can be understood as versions of synthetic aperture radar (SAR) [13] and microwave holographic imaging [14, 15] techniques, both of which involve the use of a mechanically scanned transmitter to sequentially acquire scene data. Although promising results have been achieved using these known techniques, a remaining and significant challenge is the long imaging time required due to the mechanical movement of the antennas across the sampling points over the imaging scene. Moreover, the requirement of performing a mechanical scan makes these systems expensive and difficult to manufacture. In order to address these challenges, the use of a frequency diverse metamaterial aperture was demonstrated by Hunt et al., with the goal of developing a flexible hardware framework well-suited to the implementation of advanced computational imaging concepts [16]. It was demonstrated in [16] that the use of frequency diverse metamaterial apertures could circumvent the requirement of performing a mechanical scan for the imaging. Moreover, the use of computational imaging algorithms enables image reconstruction from a reduced number of measurements, making it conceivably possible to perform video frame-rate compressive imaging with a small number of transceivers.

The metamaterial aperture consists of subwavelength resonators whose resonance frequencies are randomly distributed over the frequency range of operation. At each frequency, a different set of radiators are excited, leading to frequency diverse electromagnetic patterns that can encode the scene

Received 30 November 2014, Accepted 24 December 2014, Scheduled 19 January 2015

* Corresponding author: Okan Yurduseven (okan.yurduseven@duke.edu).

[1] Center for Metamaterials and Integrated Plasmonics, Department of Electrical and Computer Engineering, Duke University, Durham, North Carolina 27708, USA. [2] Evolv Technology, Waltham, Massachusetts 02451, USA. [3] Metamaterials Commercialization Center, Intellectual Ventures, Bellevue, Washington 98009, USA.

information onto frequency measurement modes. However, only a fraction of the metamaterial aperture is radiating at each frequency and its characteristics are not necessarily a function of its physical dimensions. This makes it difficult to compare the performance of the metamaterial aperture with other conventional imaging approaches, such as SAR. Our goal here is to better understand the characteristics and resolution limits of the metamaterial aperture by using the point spread function (PSF). The PSF provides a simple and systematic approach for characterizing the performance of the complex metamaterial aperture. Through comparison of the PSF patterns for the metamaterial aperture and a SAR system of the same dimension, the fundamental resolution limits of the frequency diverse metamaterial aperture are confirmed. The quality of the reconstructed PSF is of particular interest, especially in the presence of noise, since it is desirable to use as few measurement modes as possible to enable fast acquisition times.

This paper is organized as follows. In Section 2, the metamaterial imager and the simulation model for the metamaterial aperture are briefly described. In Section 3, the simulated PSF of the metamaterial aperture is presented and compared to the resolution limits of a SAR system of the same dimensions. Furthermore, it is demonstrated that the PSF characteristics of the metamaterial imager can be improved by using a number of advanced computational imaging algorithms. Finally, Section 4 provides concluding remarks.

2. METAMATERIAL IMAGER

The metamaterial imager (or metaimager) concept is illustrated in Figure 1. The metaimager consists of a frequency diverse square metamaterial aperture that illuminates a scene, and a low-gain probe antenna that receives the signal reflected back from the scene. The metamaterial aperture is of the size of 50 cm × 50 cm (effective panel aperture size, $L = 50$ cm), and consists of a parallel plate waveguide excited by six probe feeds. Patterned into the upper conducting plate is an array of complementary ELC (cELC) elements, whose size and spacing are significantly smaller than either the free space or guided wavelengths. The resonant frequencies of the metamaterial elements are randomly distributed over the frequency band of 17.5–26.5 GHz, covering the K-band (18–26.5 GHz). As the frequency is swept, different sets of elements are excited at each frequency point, producing complex radiation patterns that vary as a function of frequency. The diverse radiation patterns sample different spatial regions within the scene, and thus the collection of measured returns at the probe can be used to recover the scene information. We refer to the frequency-dependent radiation patterns as *measurement modes*.

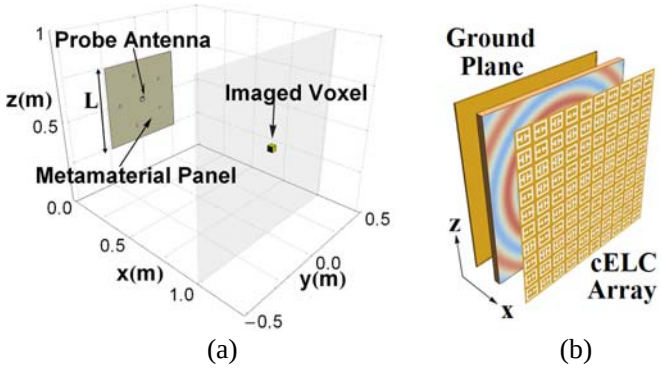

Figure 1. Illustration of the metamaterial imager. (a) Overall system consisting of a transmitting metamaterial panel (excited using six coaxial probe feeds and $L = 50$ cm) and a low-gain receiving probe antenna placed at the panel center; (b) metamaterial aperture panel.

An important parameter governing the performance of the metamaterial aperture is the quality factor (Q-factor) of the cELC unit cells within the panel. Fundamentally, the quality factor determines the number of frequency sampling points and therefore the number of measurement modes. Increasing the number of frequency sampling points beyond the limit set by the Q-factor results in strongly

correlated measurement modes, which bring little to no additional information. For the metamaterial panel demonstrated in this work, the quality factor was assumed to be 100 based on full-wave simulations. Consequently, the frequency range of 17.5–26.5 GHz was sampled at 9 MHz steps, resulting in 101 frequency points. The cELC resonators are modelled as polarizable, radiating magnetic dipoles with frequency dispersion described by a Drude-Lorentz model. The resonators couple energy from the waveguide mode to free space, with maximum coupling from a given cELC occurring approximately at its peak resonance frequency. The field illuminating the scene at each frequency is a superposition of all the magnetic dipoles. The details of the numerical model are further explained in [17]. Over a large enough bandwidth, the dispersive nature of the cELC suggests that the resulting mode patterns will likewise be dispersive; thus, the radiated field distribution within the scene space will exhibit considerable variation as a function of frequency sweep.

The field scattered from the scene at any given frequency is sampled by the probe antenna, with the field (both phase and amplitude) at the probe constituting a measurement. For the metamaterial aperture to function as an imaging system, a forward model must be implemented that describes how objects in the scene scatter the incident field, such that the collection of measurements can be inverted and the scene retrieved. Though more sophisticated models can be developed, for our purposes the first Born approximation provides a sufficient description [17, 18]. In this approximation, the field scattered from the target, E_{sca}, is simply related to the incident field, E_i, through

$$E_{sca} = f\left(\mathbf{r}_s\right) E_i \tag{1}$$

where $f(\mathbf{r}_s)$ is the target reflectivity at $\mathbf{r}_s$. A measurement matrix H that relates the measurements to the scene is then defined through the forward model. Given the frequency diverse nature of our system, we write this relationship as

$$g\left(\omega\right) = \int H\left(\omega,\, \mathbf{r}_s\right) f\left(\mathbf{r}_s\right) d\mathbf{r}_s \tag{2}$$

In (2) above, $g(\omega)$ represents a vector of measurements collected by the receiving probe and $H(\omega, \mathbf{r}_s)$ is the measurement matrix. The measurement matrix, $H(\omega, \mathbf{r}_s)$, is related to the scene through [17].

$$H\left(\omega,\, \mathbf{r}_s\right) \approx E^{tx}\left(\omega,\, \mathbf{r}_s\right) E^{rx}\left(\omega,\, \mathbf{r}_s\right) \tag{3}$$

In (3), $E^{tx}(\omega,\, \mathbf{r}_s)$ and $E^{rx}(\omega,\, \mathbf{r}_s)$ denote the fields from the transmitting metamaterial aperture panel and the receiving probe antenna projected to the point $\mathbf{r}_s$, respectively.

3. POINT SPREAD FUNCTION AND IMAGE RECONSTRUCTION

When reconstructing the target information, its exact location is unknown. As a result, the scene is discretized into N voxels. If the frequency sweep is sampled at M frequency points, (2) becomes a finite dimension matrix equation as follows

$$g_M = H_{M\times N} f_N \tag{4}$$

Because the measurement matrix is not necessarily square, there is no well-defined inverse for the matrix Equation (4), and thus the scene must be estimated using computational methods. While these methods can obtain decent images [17], they make extra assumptions about the scene. In order to prevent such issues, matched filter reconstruction can be used [19], in which an estimate of f can be obtained from

$$f_{est} = H^{\dagger} g \tag{5}$$

where $H^{\dagger}$ denotes the conjugate transpose of the measurement matrix H. From (4) and (5), we see that the relationship of the actual scene vector without any simplifying assumptions (the "truth") and the estimated scene vector is

$$f_{est} = H^{\dagger} H f = h f \tag{6}$$

so that the quantity $h = H^{\dagger}H$ can be considered the transfer matrix for the system. It can be expected that the transfer matrix h will be characterized by a PSF, which will include all aberrations due to aperture and diffraction limits. Therefore, an appropriate approach to understanding the imaging characteristics of the metamaterial aperture is to study the properties of the PSF corresponding to sub-diffraction limited voxels in the scene.

3.1. Resolution Using Matched Filter Reconstruction Algorithm

As a benchmark, we consider the imaging of a single voxel at a distance of $d = 1$ m using one transmitting metamaterial panel and one receiving probe placed at the center of the panel as illustrated in Figure 1(a). Images reconstructed using the matched filter reconstruction algorithm are shown in Figure 2 for signal-to-noise ratios (SNRs) of infinite (no noise), 20 dB, 10 dB and 1 dB.

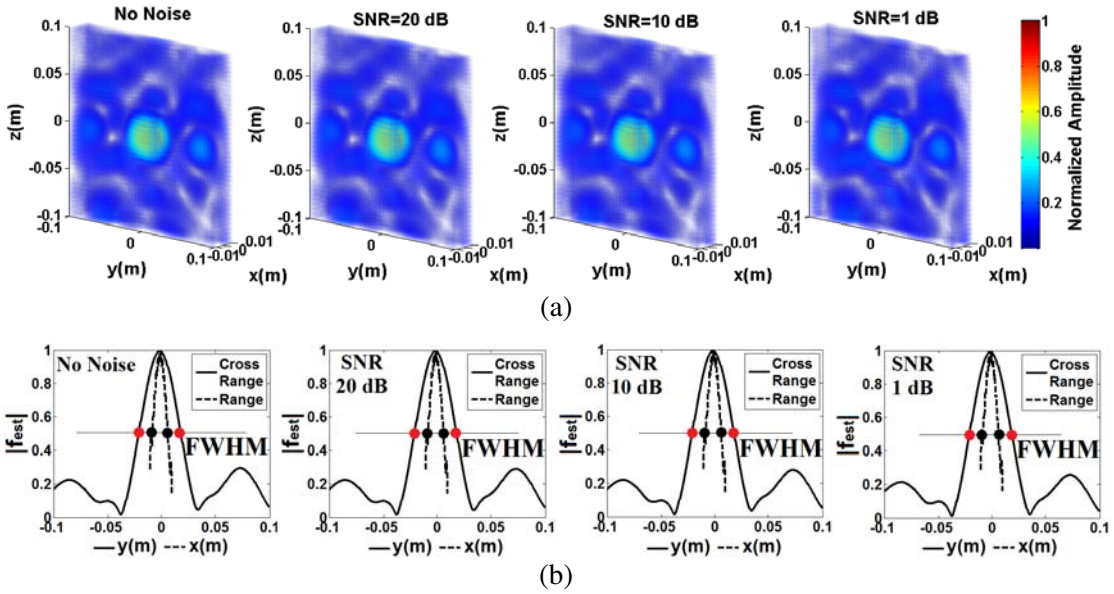

Figure 2. Reconstructed images of a point target using the matched filter reconstruction method. (a) Three-dimensional PSF patterns; (b) range (x-z plane) and cross-range (y-z plane) PSF curves of the metamaterial panel with the FWHM points highlighted (red dots: cross-range FWHM; black dots: range FWHM).

In order to model various SNR levels, noise was added to measured signal through $g_n = g + n(\sigma)$ where g_n is the noisy measurement, and $n(\sigma)$ is the added noise which is sampled from a Gaussian identical independent distribution with zero mean and variance of $\sigma^2 = \text{SNR}|g|$. Here, we have defined noise with respect to the average of the received signal over all frequencies, $|g|$. As expected, the reconstructed PSF patterns shown in Figure 2(a) do not vary with noise since matched filter reconstruction is robust to noise. As demonstrated in Figure 2(b), the resolution of the metamaterial aperture is taken here as the distance between the points in the PSF pattern with an amplitude of 50% of the normalized maximum PSF amplitude (−3 dB on logarithmic scale), or the full-width at half-maximum (FWHM), in range (x-z plane) and cross-range (y-z plane). Applying the FWHM criterion in Figure 2(b), the measured resolutions in range and cross-range are 2.24 cm and 3.46 cm, respectively. While these numbers serve as an estimate of the resolution possible with the metamaterial aperture at $d = 1$ m, these limits can be placed into context by comparing them with the resolution limits of a SAR system. For this purpose, we consider a transmitting SAR aperture with the same dimensions as the metamaterial aperture and operating over the same frequency bandwidth. The receiver is assumed to be the same low-gain receiving probe as in the metamaterial imaging system. Since the metamaterial aperture radiates in almost all directions, we consider a strip map SAR system. With these assumptions, the resolution of the SAR system at $d = 1$ m would be 1.66 cm in range and 2.72 cm in cross-range, respectively, using the following SAR resolution equations [13].

$$\delta_r = \frac{c}{2B} \tag{7}$$

and

$$\delta_{cr} = \frac{\lambda R}{L_{eff}} \tag{8}$$

In (7) and (8), δ_r and δ_{cr} denote the resolution limits in range and cross-range, respectively, while λ is the wavelength, B is the imaging bandwidth, L_{eff} is the effective aperture size of the SAR imaging system and R is the distance between the imager and the imaged object. It can be seen in (7) and (8) that the range resolution is determined by the bandwidth of the imager while the cross-range resolution is a function of the aperture size of the imager.

The resolution limits of the SAR system appear to be better than that of the metamaterial aperture using the matched filter reconstruction algorithm. The metamaterial panels simulated here support a total number of measurement modes equal to $M = 606$, which is the product of the number of frequency sweep points, 101, and the number of coaxial probe feeds feeding the metamaterial panel, 6. In this work, the imaging scene is three-dimensional and discretized into 5 mm cubic voxels, selected to be smaller than the half-wavelength over the imaging frequency band of 17.5–26.5 GHz. The dimensions of the imaging scenes demonstrated in Figure 2 are 2.5 cm (x-axis) $\times$ 20 cm (y-axis) $\times$20 cm (z-axis), resulting in $N = 8000$ voxels.

Comparing the total number of measurement modes, M, and number of voxels into which the scene was discretized, N, it is evident that the scene is significantly undersampled ($M < N$). Moreover, due to the random composition of these modes and the fact that they are inherently correlated through frequency diversity, it can be expected there will be overlap in the mode patterns, such that the effective number of modes will be smaller than $M = 606$. A plot of the singular value spectrum reveals this correlation. From Figure 3, it is clear that scene is undersampled by a considerable amount, and unquestionably so in the presence of noise.

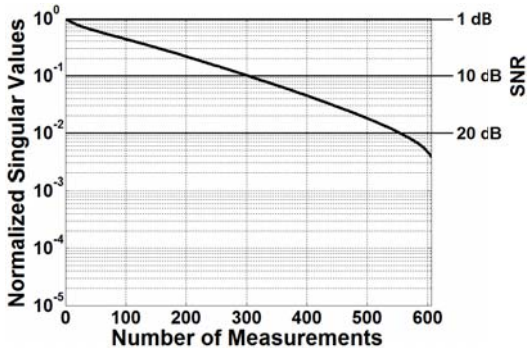

Figure 3. Singular value spectra for the metamaterial imager. The scene is taken to be 1 m away from the aperture, with a field-of-view of $\pm 10^\circ$ for both azimuth and elevation angles.

While the proposed frequency diverse metamaterial aperture yields lower resolutions compared to SAR system of the same dimensions, it should be emphasized that the metamaterial aperture allows us to encode the scene information into frequency measurement modes, circumventing the need for mechanical scans. This is not possible in most SAR imaging systems. In order to compensate for the low resolution, we can use more advanced computational imaging algorithms. In the next section, we will see how more advanced techniques can obtain resolutions similar to SAR systems.

3.2. Resolution Using Advanced Computational Imaging Algorithms

Since the scene is undersampled, a least-squares approach can conceivably make better use of the information to estimate the scene. Least-squares techniques pose the solution of (4) as the L2 norm optimization problem $\|g - Hf\|_2^2$ subject to various constraint or objective functions. The conjugate gradient square (CGS) method is an iterative least-squares type of approach [20]. As a comparison, we apply the CGS method on the exact same data set as in Figure 2, recovering the PSF patterns shown in Figure 4. In the CGS algorithm the matched filter result is taken as a starting estimate, with a non-linear iterative scheme then applied to optimally converge to the most likely scene from the set of available measurements. At each iteration, the residual of the objective function $\|g - Hf\|_2^2$ is calculated and the iteration continues until either the total iteration number or the desired minimum residual level

(selected to be 0.001 in this work), criterion is satisfied. As can be seen in Figure 4(a), the recovered PSF patterns using the CGS reconstruction algorithm clearly resemble the expected classical airy-like pattern, with the PSF main lobes fully resolved at all SNR levels and the side lobes fully resolved above the SNR level of 10 dB. Applying the FWHM criterion in Figure 4(b), we find the implied resolution of the metamaterial imager is 2 cm in range and 2.78 cm in cross-range. As can be seen in Figure 4(a), the CGS reconstruction algorithm is sensitive to noise. This is due to the fact that the singular values below the noise level (see Figure 3) are dominated by noise. Since the CGS reconstruction algorithm is a least-square solver, the estimate is proportional to the inverse of the singular values, and therefore, the effect of noise is magnified. However, it should be noted here that as the SNR is reduced from infinite (no noise) to 1 dB in Figure 4(b), the width of the PSF main lobe (and therefore the FWHM) remains the same, suggesting that the resolution of the metamaterial imager does not change as a function of noise.

The obtained resolution of the metaimager is close to that of a SAR system of the same dimension, calculated as 1.66 cm in range and 2.72 cm in cross-range using (7) and (8). Comparing the range and cross-range FWHMs obtained using the matched filter method in Figure 2(b) and the CGS reconstruction algorithm in Figure 4(b), it can be seen that narrower FWHMs (and therefore better resolution) are obtained using the CGS algorithm. Finally, for sparse scenes, imaging techniques that minimize with respect to the L1 norm can also be applied. Here, we make use of the two-step iterative shrinkage/thresholding (TwIST) algorithm [21]. As demonstrated in Figure 4(c), the TwIST algorithm

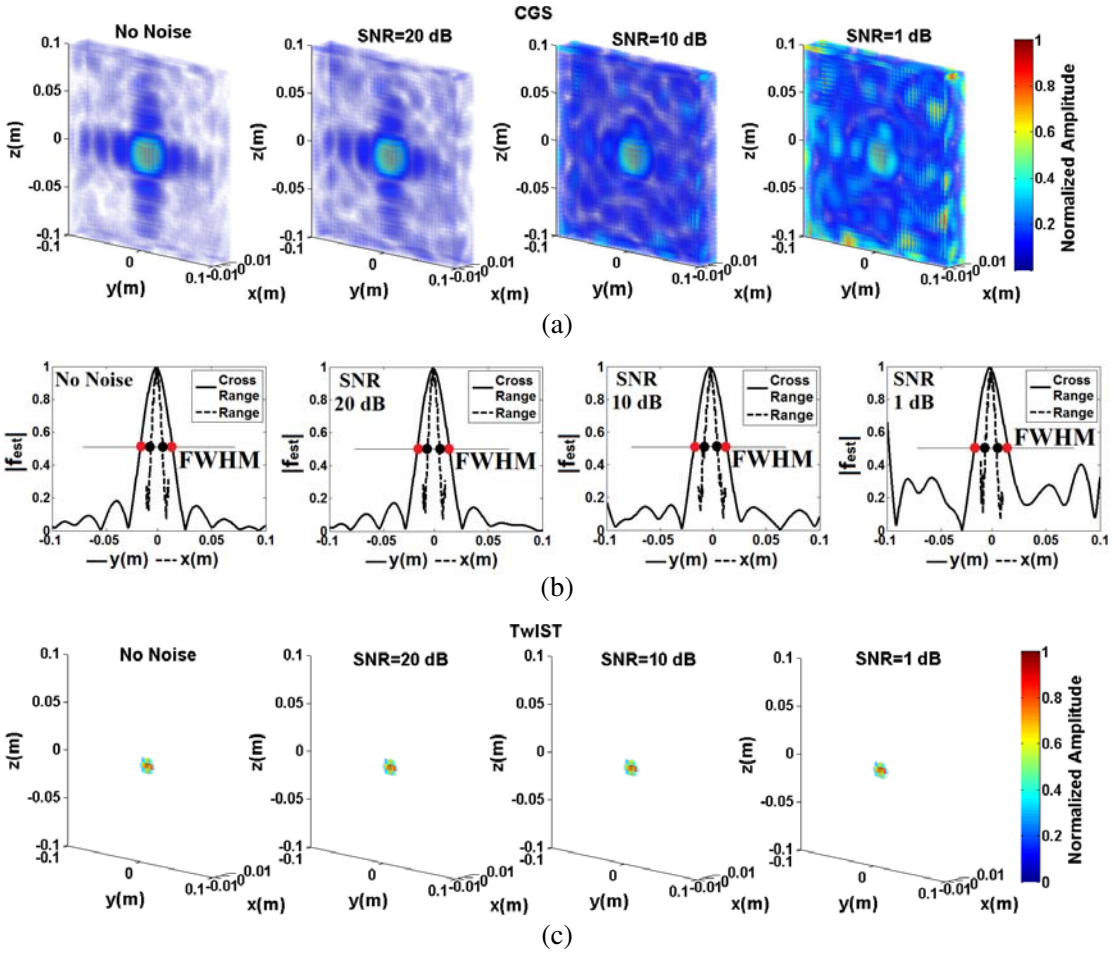

Figure 4. Reconstructed images of a point target. (a) Three-dimensional PSF patterns using the CGS reconstruction algorithm; (b) range (x-z plane) and cross-range (y-z plane) PSF curves of the metamaterial panel with the FWHM points are highlighted (red dots: cross-range FWHM; black dots: range FWHM); (c) reconstructed three-dimensional images of the voxel using the TwIST algorithm.

fully resolves the imaged voxel thanks to the sparsity of the imaged scene.

In order to investigate the ability of the metamaterial imager to resolve multiple point sources (voxels) in range and cross-range, we constructed two multi-voxel targets. According to the PSF patterns examined, if we place the voxels such that their separation is larger than the FWHM, we should be able to resolve them. To this end, the first constructed target consists of five voxels in cross-range; two positioned along the y-axis, two positioned along the z-axis, and one positioned at the origin. As demonstrated in Figure 5(a), the plane containing the cross-range multi-voxel target was situated a distance of $d = 1$ m from the metamaterial panel. The distance between the cross-range voxels was chosen according to cross-range resolution of the metaimager. In view of this, the distance between the voxels was chosen to be 4 cm, which is slightly larger than the cross-range FWHM of 2.78 cm in order to fully resolve the individual PSFs. The SNR level for the imaging was varied in the range of infinite (no noise) to 1 dB, and the image reconstruction was performed using the CGS algorithm. The reconstructed images of the cross-range multi-voxel target are shown in Figure 5(b).

As illustrated in Figure 5(b), as a result of imaging five voxels, five PSFs each corresponding to each voxel in the imaging scene are obtained above the SNR level of 10 dB. In comparison to the reconstructed images of a single voxel target demonstrated in Figure 4(a), it can be seen in Figure 5(b) that the reconstructed image of the multi-voxel target is significantly deteriorated with no resolved PSFs when the SNR level is reduced to 1 dB. This is due to the fact that for a simple target, such as a single voxel in Figure 4(a), the effective measurement modes remaining above 1 dB SNR in Figure 3 are enough to capture the required spectral information for imaging. However, as the target becomes more complex as with the multi-voxel target, there is more information in the scene and the same number of measurement modes at 1 dB SNR is not enough to capture the spectral information.

The second multi-voxel target has two voxels in range along the x-axis. In Figure 6(a), the imaging of a range multi-voxel target is demonstrated. As can be seen in Figure 6(a), the target consists of two voxels, placed at distances of $d = 0.9985$ m and $d = 1.0015$ m from the panel. The distance between the two voxels corresponds to a 3 cm range separation along the x-axis which was selected to be slightly

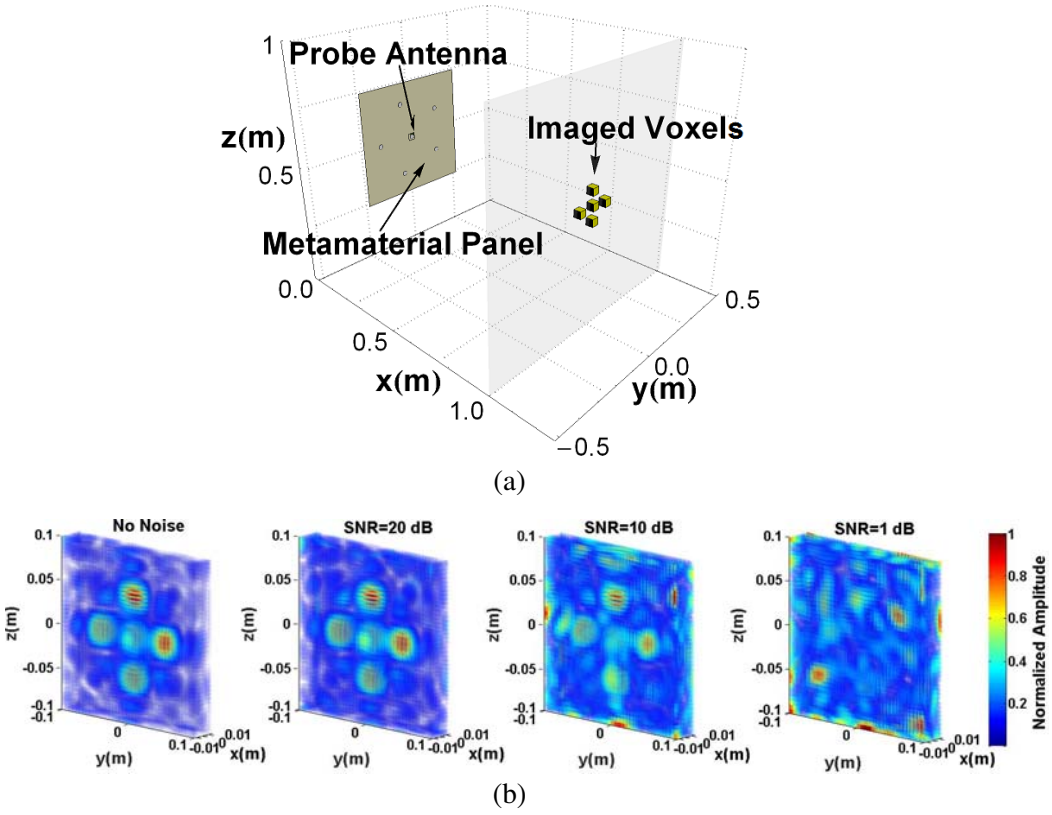

Figure 5. Imaging of a cross-range multi-voxel target consisting of five voxels. (a) Metaimager configuration; (b) reconstructed three-dimensional images using the CGS reconstruction algorithm.

larger than the range FWHM (2 cm) of the metaimager obtained using the CGS reconstruction algorithm in order to fully resolve the individual PSFs. It should be noted that the imaging of these voxels would not be possible in practice due to their placement with respect to each other (the second voxel is in the shadow of the first voxel). However, the first Born approximation in our simulated forward model assumes that there are no second order effects, making such a simulation possible. As illustrated in Figure 6(b), the PSFs of the voxels in range have been successfully resolved above the SNR level of 10 dB. Reducing the SNR level below 10 dB results in a considerable increase in the sidelobe levels and degrades the image reconstruction due to the reduced number of effective measurement modes according to Figure 3. Similar to the imaging of the cross-range multi-voxel target, the imaging of the range multi-voxel target requires more spectral information to be captured in comparison to the imaging of the single voxel target demonstrated in Figure 4(a).

Noise robustness of the CGS reconstruction algorithm can be improved by using a regularization parameter for the reconstruction. It should be emphasized that the need for regularizer is an attribute of the computational imaging technique used, CGS, and is not a consequence of the metamaterial aperture. Similar problems can be seen when applying such techniques to SAR imaging. The regularized objective function for the CGS reconstruction algorithm can be given as follows

$$\left\| H^{\dagger} g - \left(H^{\dagger} H + \mu I \right) f \right\|_2^2 \tag{9}$$

In (9), I is an identity matrix and μ is the regularization parameter, which is calculated as

$$\mu = k\xi(H) \tag{10}$$

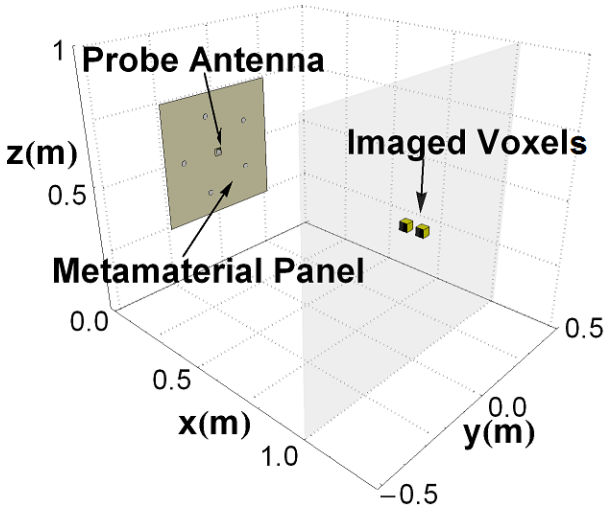

(a)

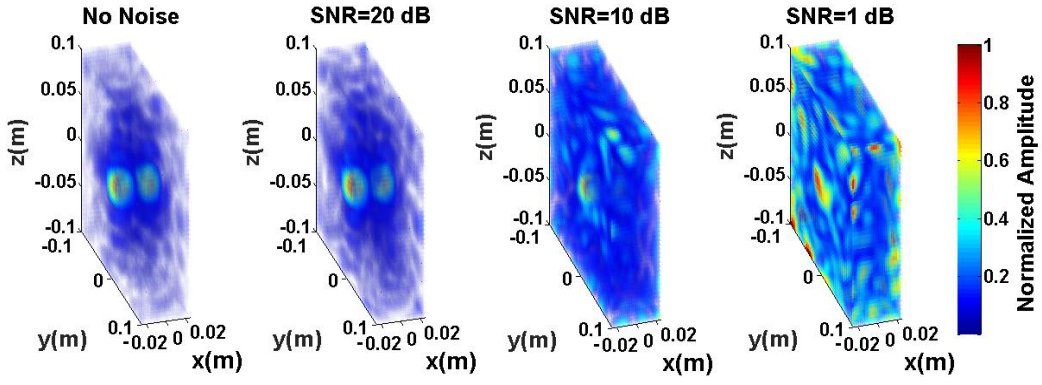

(b)

Figure 6. Imaging of a range multi-voxel target consisting of two voxels. (a) Metaimager configuration; (b) reconstructed three-dimensional images using the CGS reconstruction algorithm.

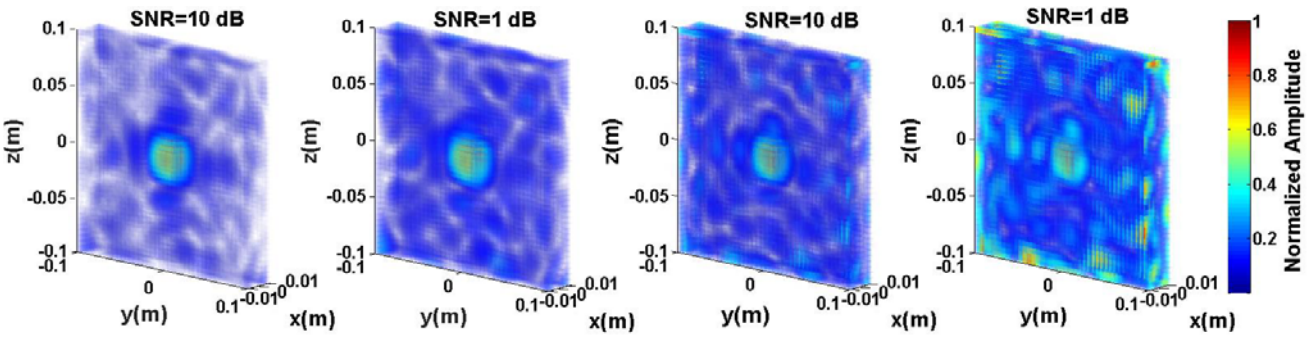

Figure 7. Imaging of a single voxel target using CGS reconstruction algorithm with and without regularization. With regularization: (a) SNR = 10 dB; (b) SNR = 1 dB; without regularization: (c) SNR = 10 dB; (d) SNR = 1 dB.

In (10), $\xi(H)$ denotes the maximum singular value of the measurement matrix H while k is a parametrically optimized regularization constant, which was found to be optimal when set to 10^{-4}. In this context, the regularization parameter μ works as a filter eliminating the singular values of the H matrix smaller than its value, improving the condition number of the H matrix. This makes the imaging more robust to noise. As can be seen in (9), increasing the regularization parameter μ results in the regularized CGS reconstruction converging to the matched filter reconstruction given in (5) while decreasing it makes the regularization effect negligible. Following the determination of the regularization parameter, the imaging of a single voxel target was done using the CGS reconstruction algorithm at SNR levels of 1 dB and 10 dB with and without regularization. The reconstructed images are shown in Figure 7.

Comparing the images reconstructed at an SNR level of 10 dB in Figure 7 it can be seen that the reconstructed PSF with regularization has a clear outline and almost fully resolved sidelobes in comparison to the reconstructed image with no regularization is applied. Similarly, the PSF reconstructed at 1 dB SNR is more robust to noise and is of better quality in comparison to the reconstructed PSF without regularization. However, it is evident in Figure 7 that although the noise robustness of the CGS algorithm was improved as a result of regularizing the CGS reconstruction, the main lobes of the reconstructed PSFs (and therefore the FWHM widths) are wider in comparison to the CGS reconstruction without regularization (by a factor of 13.3%). This is due to the convergence of the CGS reconstruction to the matched filter reconstruction when the regularization is applied according to (9).

4. CONCLUSION

The resolution of a frequency diverse metamaterial aperture has been studied. It has been demonstrated that the metamaterial imager consisting of a metamaterial transmitting panel of size 0.5 m × 0.5 m has resolution of 2.24 cm in range and 3.46 cm in cross-range when matched filter reconstruction algorithm is used without any assumptions. Using more advanced computational imaging algorithms, such as least-squares, the resolution of the metamaterial imager has been improved to 2 cm in range and 2.78 cm in cross-range. The obtained resolution of the frequency diverse metamaterial imager is comparable with the resolution of a SAR aperture of the same dimensions, which has been calculated to be 1.66 cm in range and 2.72 cm in cross-range. The demonstrated metamaterial imager offers the advantages of circumventing the mechanical scan requirement for the imaging and being able to perform the image reconstruction in a compressive manner using reduced number of measurements in comparison to traditional SAR imaging techniques. We have shown that using more advanced computational imaging techniques, such as a simple least-squares reconstruction, or CGS, allows the performance of the metamaterial aperture to be on par with SAR systems, without the need for time consuming expensive mechanical scanning. The results demonstrated in this paper lay the foundation for new studies into how the resolution of frequency diverse imaging systems can be further improved.

ACKNOWLEDGMENT

This work was supported by the Department of Homeland Security, Science & Technology Directorate (Contract No. HSHQDC-12-C-00049). The published material represents the position of the author(s) and not necessarily that of the DHS.

REFERENCES

1. Nikolova, N. K., "Microwave imaging for breast cancer," *IEEE Microwave Magazine*, Vol. 12, No. 7, 78–94, Dec. 2011.
2. Elsdon, M., O. Yurduseven, and D. Smith, "Early stage breast cancer detection using indirect microwave holography," *Progress In Electromagnetics Research*, Vol. 143, 405–419, 2013.
3. Grzegorczyk, T. M., P. M. Meaney, P. A. Kaufman, R. M. di Florio-Alexander, and K. D. Paulsen, "Fast 3-D tomographic microwave imaging for breast cancer detection," *IEEE Transactions on Medical Imaging*, Vol. 31, No. 8, 1584–1592, Aug. 2012.
4. Bindu, G. N., S. J. Abraham, A. Lonappan, V. Thomas, C. K. Aanandan, and K. T. Mathew, "Active microwave imaging for breast cancer detection," *Progress In Electromagnetics Research*, Vol. 58, 149–169, 2006.
5. Wang, Y. and A. E. Fathy, "Advanced system level simulation platform for three-dimensional UWB through-wall imaging SAR using time-domain approach," *IEEE Transactions on Geoscience and Remote Sensing*, Vol. 50, No. 5, 1986–2000, May 2012.
6. Ahmad, F., M. G. Amin, and S. A. Kassam, "Synthetic aperture beamformer for imaging through a dielectric wall," *IEEE Transactions on Aerospace and Electronic Systems*, Vol. 41, No. 1, 271–283, Jan. 2005.
7. Dehmollaian, M., M. Thiel, and K. Sarabandi, "Through-the-wall imaging using differential SAR," *IEEE Transactions on Geoscience and Remote Sensing*, Vol. 47, No. 5, 1289–1296, May 2009.
8. Yang, Y., C. Zhang, and A. E. Fathy, "Development and implementation of ultra-wideband see-through-wall imaging system based on sampling oscilloscope," *IEEE Antennas and Wireless Propagation Letters*, Vol. 7, 465–468, 2008.
9. Yurduseven, O., "Indirect microwave holographic imaging of concealed ordnance for airport security imaging systems," *Progress In Electromagnetics Research*, Vol. 146, 7–13, 2014.
10. Sheen, D. M., D. L. McMakin, and T. E. Hall, "Three-dimensional millimeter-wave imaging for concealed weapon detection," *IEEE Transactions on Microwave Theory and Techniques*, Vol. 49, No. 9, 1581–1592, Sep. 2001.
11. Demirci, S., H. Cetinkaya, E. Yigit, C. Ozdemir, and A. A. Vertiy, "A study on millimeter-wave imaging of concealed objects: Application using back-projection algorithm," *Progress In Electromagnetics Research*, Vol. 128, 457–477, 2012.
12. Martinez-Lorenzo, J. A., F. Quivira, and C. M. Rappaport, "SAR imaging of suicide bombers wearing concealed explosive threats," *Progress In Electromagnetics Research*, Vol. 125, 255–272, 2012.
13. Moreira, A., P. Prats-Iraola, M. Younis, G. Krieger, I. Hajnsek, and K. P. Papathanassiou, "A tutorial on synthetic aperture radar," *IEEE Geoscience and Remote Sensing Magazine*, Vol. 1, No. 1, 6–43, Mar. 2013.
14. Smith, D., O. Yurduseven, B. Livingstone, and V. Schejbal, "Microwave imaging using indirect holographic techniques," *IEEE Antennas and Propagation Magazine*, Vol. 56, No. 1, 104–117, Feb. 2014.
15. Amineh, R. K., J. McCombe, and N. K. Nikolova, "Microwave holographic imaging using the antenna phaseless radiation pattern," *IEEE Antennas and Wireless Propagation Letters*, Vol. 11, 1529–1532, 2012.
16. Hunt, J., T. Driscoll, A. Mrozack, G. Lipworth, M. Reynolds, D. Brady, and D. R. Smith, "Metamaterial apertures for computational imaging," *Science*, Vol. 339, No. 6117, 310–313, Jan. 2013.

17. Lipworth, G., A. Mrozack, J. Hunt, D. Marks, T. Driscoll, D. Brady, and D. R. Smith, "Metamaterial apertures for coherent computational imaging on the physical layer," *Journal of the Optical Society of America A*, Vol. 30, No. 8, 1603–1612, Aug. 2013.
18. Hunt, J., J. Gollub, T. Driscoll, G. Lipworth, A. Mrozack, M. Reynolds, D. Brady, and D. Smith, "Metamaterial microwave holographic imaging system," *Journal of the Optical Society of America A*, Vol. 31, 2109–2119, 2014.
19. Kay, S. M., *Fundamentals of Statistical Signal Processing, Volume II: Detection Theory*, Prentice Hall Signal Processing Series, New Jersey, 1998.
20. Barrett, R., M. Berry, T. F. Chan, J. Demmel, J. Donato, J. Dongarra, V. Eijkhout, R. Pozo, C. Romine, and H. van der Vorst, *Templates for the Solution of Linear Systems: Building Blocks for Iterative Methods*, 1st Edition, 12–31, Society for Industrial and Applied Mathematics, Philadelphia, PA, USA, 1987.
21. Bioucas-Dias, J. M. and M. A. T. Figueiredo, "A new TwIST: Two-step iterative shrinkage/thresholding algorithms for image restoration," *IEEE Transactions on Image Processing*, Vol. 16, No. 12, 2992–3004, Dec. 2007.